A Forward semi-Lagrangian Method for the Numerical Solution of the Vlasov Equation

Nicolas Crouseilles, Thomas Respaud, Eric Sonnendrücker

INRIA

INSTITUT NATIONAL DE RECHERCHE EN INFORMATIQUE ET EN AUTOMATIQUE

A Forward semi-Lagrangian Method for the Numerical Solution of the Vlasov Equation

Nicolas Crouseilles — Thomas Respaud — Eric Sonnendrücker

N° 6727

Novembre 2008

Thème NUM

ISSN 0249-6399 ISRN INRIA/RR--6727--FR+ENG

INSTITUT NATIONAL
DE RECHERCHE
EN INFORMATIQUE
ET EN AUTOMATIQUE

INRIA

centre de recherche
NANCY - GRAND EST

A Forward semi-Lagrangian Method for the Numerical Solution of the Vlasov Equation

Nicolas Crouseilles*, Thomas Respaud †, Eric Sonnendrücker ‡

Thème NUM — Systèmes numériques
Équipe-Projet Calvi

Rapport de recherche n° 6727 — Novembre 2008 — 24 pages

Abstract: This work deals with the numerical solution of the Vlasov equation. This equation gives a kinetic description of the evolution of a plasma, and is coupled with Poisson's equation for the computation of the self-consistent electric field. The coupled model is non linear. A new semi-Lagrangian method, based on forward integration of the characteristics, is developed. The distribution function is updated on an eulerian grid, and the pseudo-particles located on the mesh's nodes follow the characteristics of the equation forward for one time step, and are deposited on the 16 nearest nodes. This is an explicit way of solving the Vlasov equation on a grid of the phase space, which makes it easier to develop high order time schemes than the backward method.

Key-words: Semi-Lagrangian method, Runge-Kutta, plasma simulation, Vlasov equation

* INRIA-Nancy-Grand Est, CALVI Project
† IRMA Strasbourg et INRIA-Nancy-Grand Est, CALVI Project
‡ IRMA Strasbourg et INRIA-Nancy-Grand Est, CALVI Project

Centre de recherche INRIA Nancy – Grand Est
LORIA, Technopôle de Nancy-Brabois, Campus scientifique,
615, rue du Jardin Botanique, BP 101, 54602 Villers-Lès-Nancy
Téléphone : +33 3 83 59 30 00 — Télécopie : +33 3 83 27 83 19

Une méthode semi-Lagrangienne en avant pour la résolution numérique de l'équation de Vlasov

Résumé : Ce document concerne la résolution numérique de l'équation de Vlasov qui est un modèle cinétique permettant de décrire l'évolution d'un plasma. Elle est couplée à une équation, par exemple l'équation de Poisson, permettant le calcul des champs auto-consistants. Le modèle couplé est non linéaire. Nous proposons ici une nouvelle méthode semi-Lagrangienne dans laquelle les caractéristiques sont intégrées en avant, dans le sens du temps, contrairement à la méthode semi-Lagrangienne classique qui intègre les caractéristiques en arrière. L'autre ingrédient de la méthode semi-Lagrangienne est une technique de déposition de l'information portée par les particules sur une grille. Celle-ci est basée sur un produit tensoriel de splines cubiques de sorte qu'en deux dimensions la formule de déposition implique 16 points de la grille. Grâce à cette nouvelle technique la méthode semi-Lagrangienne devient complètement explicite et peut s'appuyer sur des solveurs numériques d'équations différentielles classiques, rendant ainsi plus simple la montée en ordre en temps. La méthode est validée sur plusieurs cas tests représentatifs des problèmes réalistes basés sur ce modèle.

Mots-clés : méthode semi-Lagrangienne, Runge-Kutta, simulation de plasmas, équation de Vlasov

1 Introduction

Understanding the dynamics of charged particles in a plasma is of great importance for a large variety of physical phenomena, such as the confinement of strongly magnetized plasmas, or laser-plasma interaction problems for example. Thanks to recent developments in computational science and in numerical methods, meaningful comparisons between experience and numerics are becoming possible.

An accurate model for the motion of charged particles, is given by the Vlasov equation. It is based on a phase space description so that non-equilibrium dynamics can accurately be investigated. The unknown $f(t, x, v)$ depends on the time t, the space x and the velocity v. The electromagnetic fields are computed self-consistently through the Maxwell or Poisson equations, which leads to the nonlinear Vlasov-Maxwell or Vlasov-Poisson system.

The numerical solution of such systems is most of the time performed using Particle In Cell (PIC) methods, in which the plasma is approximated by macro-particles (see [3]). They are advanced in time with the electromagnetic fields which are computed on a grid. However, despite their capability to treat complex problems, PIC methods are inherently noisy, which becomes problematic when low density or highly turbulent regions are studied. Hence, numerical methods which discretize the Vlasov equation on a grid of the phase space can offer a good alternative to PIC methods (see [5, 8, 9, 19, 4]). The so-called Eulerian methods can deal with strongly nonlinear processes without additional complexity, and are well suited for parallel computation (see [12]). Moreover, semi-Lagrangian methods which have first been introduced in meteorology (see [18, 21, 22]), try to take advantage of both Lagrangian and Eulerian approaches. Indeed, they allow a relatively accurate description of the phase space using a fixed mesh and avoid traditional step size restriction using the invariance of the distribution function along the trajectories. Standard semi-Lagrangian methods calculate departure points of the characteristics ending at the grid point backward in time; an interpolation step enables to update the unknown.

In this work, we consider the numerical resolution of the two-dimensional Vlasov equation on a mesh of the phase space using a forward semi-Lagrangian numerical scheme. In the present method, the characteristics curves are advanced in time and a deposition procedure on the phase space grid, similar to the procedure used in PIC methods for the configuration space only, enables to update the distribution function.

One of the main cause for concern with semi-Lagrangian methods, is computational costs. With Backward semi-Lagrangian methods (BSL), the fields have to be computed iteratively, with Newton fixed point methods, or prediction correction algorithms. This is due to an implicit way of solving the characteristics (see [19] for details). This strategy makes high order resolution quite difficult and expensive. Making the problem explicit enables to get rid of iterative methods for the characteristics, and to use for example high order Runge Kutta methods more easily. This is one of the main advantages of the present Forward semi-Lagrangian (FSL) method. Once the new position of the particles computed, a remapping (or a deposition) step has to be performed. This issue is achieved using cubic spline polynomials which deposit the contribution of the Lagrangian particles on the uniform Eulerian mesh. This step is similar to the deposition step which occurs in PIC codes but in our case, the deposition is performed in all the phase space grid. Similarities can also be found in strategies developed in [6, 14, 16] for meteorology applications.

In order to take benefit from the advantages of PIC and semi-Lagrangian methods, and since the two methods (PIC and FSL) really look like each other, except the deposition step, we have also developed a hybrid method, where the deposition step is not performed at each time step, but every T time steps. During the other time steps, the fields are computed directly at the new position of the particles. It shall be noticed that however the present method is not a real PIC method, since the particle weights are not constant. Indeed, in this method based on a description of the unknown using cubic spline polynomials, the spline coefficients play the role of the particle weights, and are updated at each time step. This kind of hybrid approach has been developed recently in a slightly different framework in [20] inspired by [7].

This paper is organized as follows. In the next section, the two Vlasov equations which will be dealt with are presented. Then, we shall introduce the Forward semi-Lagrangian (FSL) method, always regarding it comparatively to Backward semi-Lagrangian (BSL) methods. Afterward, numerical results for several test cases are shown and discussed. Eventually, some specific details are given in two appendices, one for the computation of an exact solution to the Landau damping problem, and the other about the solution of the Poisson equation for the Guiding-Center model.

2 Models in plasma physics

In this section, we briefly present two typical reduced models from plasma physics for the description of the time evolution of charged particles. These two-dimensional models are relevant for more complex problems we are interested in and shall be used to validate our new method.

2.1 Vlasov-Poisson model

We consider here the classical 1D Vlasov-Poisson model, the unknown of which $f = f(t, x, v)$ is the electron distribution function. It depends on the space variable $x \in [0, L]$ where $L > 0$ is the size of the domain, the velocity variable $v \in \mathbb{R}$ and the time $t \geq 0$. The Vlasov equation which translates the invariance of the distribution function along the characteristics then writes

$$\frac{\partial f}{\partial t} + v\partial_x f + E(t, x)\partial_v f = 0, \tag{2.1}$$

with a given initial condition $f(0, x, v) = f_0(x, v)$. The self-consistent electric field $E(t, x)$ is computed thanks to the distribution function f

$$\partial_x E(t, x) = \int_{\mathbb{R}} f(t, x, v)dv - \rho_i, \quad \int_0^L E(t, x)\mathrm{d}x = 0, \tag{2.2}$$

where ρ_i denotes the ion density which forms a uniform and motionless background in the plasma.

The Vlasov-Poisson model constitutes a nonlinear self-consistent system as the electric field determines f with (2.1) and is in turn determined by it in (2.2). It presents several conserved quantities as the total number of particles, the L^p norms ($p \geq 1$) defined by $\|f\|_{L^p} = (\iint |f|^p dxdv)^{1/p}$, the momentum and the total energy, as follows:

$$\begin{aligned} \frac{d}{dt}\iint f(t, x, v)dxdv = \frac{d}{dt}\|f(t)\|_{L^p} &= \frac{d}{dt}\iint v f(t, x, v)dxdv \\ &= \frac{d}{dt}\left[\iint v^2 f(t, x, v)dxdv + \int E(t, x)^2 dxdv\right] \\ &= 0. \end{aligned}$$

One of the main features of the present work is to develop accurate numerical methods which are able to preserve these exactly or approximately these conserved quantities for long times.

2.2 Guiding-center model

We are also interested in other kinds of Vlasov equations. For instance, in the guiding-center approximation. Charged particles in magnetized tokamak plasmas can be modeled by the density $f = f(t, x, y)$ in the 2 dimensional poloidal plane by

$$\frac{\partial f}{\partial t} + E^{\perp}(x, y) \cdot \nabla f = 0, \tag{2.3}$$

coupled self-consistently to Poisson's equation for the electric field which derives from a potential $\Phi = \Phi(x, y)$

$$-\Delta\Phi(t, x, y) = f(t, x, y), \quad E(t, x, y) = -\nabla\Phi(t, x, y). \tag{2.4}$$

In equation (2.3), the advection term $E^{\perp} = (E_y, -E_x)$ depends on (x, y) and the time-splitting cannot be simply applied like in the Vlasov-Poisson case. Hence, this simple model appears to be interesting in order to test numerical methods.

The guiding-center model (2.3)-(2.4) also presents conserved quantities as the total number of particles and L^2 norm of f (energy) and E (enstrophy)

$$\frac{d}{dt}\iint f(t, x, y)dxdy = \frac{d\|f(t)\|_{L^2}^2}{dt} = \frac{d\|E(t)\|_{L^2}^2}{dt} = 0. \tag{2.5}$$

2.3 Characteristic curves

We can re-write Vlasov equations in a more general context by introducing the characteristic curves

$$\frac{dX}{dt} = U(X(t), t). \tag{2.6}$$

Let us introduce $X(t, x, s)$ as the solution of this dynamical system, at time t whose value is x at time s. These are called the characteristics of the equation. With $X(t)$ a solution of (2.6), we obtain:

$$\frac{d}{dt}(f(X(t), t)) = \frac{\partial f}{\partial t} + \frac{dX}{dt} \cdot \nabla_X f = \frac{\partial f}{\partial t} + U(X(t), t) \cdot \nabla_X f = 0. \tag{2.7}$$

which means that f is constant along the characteristics. Using these notations, it can be written

$$f(X(t; x, s), t) = f(X(s; x, s), s) = f(x, s)$$

for any times t and s, and any phase space coordinate x. This is the key property used to define semi-Lagrangian methods for the solution of a discrete problem.

3 The forward semi-Lagrangian method

In this section, we present the different stages of the forward semi-Lagrangian method (FSL) and try to emphasize the differences with the traditional backward semi-Lagrangian method (BSL).

3.1 General algorithm

Let us consider a grid of the studied space (possibly phase-space) with N_x and N_y the number of points in the x direction $[0, L_x]$ and in the y direction $[0, L_y]$. We then define

$$\Delta x = L_x/N_x, \quad \Delta y = L_y/N_y, \quad x_i = i\Delta x, \quad y_j = j\Delta y,$$

for $i = 0, .., N_x$ and $j = 0, .., N_y$. One important point of the present method is the definition of the approximate distribution functions which are projected on a cubic B-splines basis:

$$f(t, x, y) = \sum_{k,l} \omega^n_{k,l} S(x - X_1(t; x_k, y_l, t^n)) S(v - X_2(t; x_k, y_l, t^n)), \tag{3.8}$$

where $X(t; x_k, y_l, t^n) = (X_1, X_2)(t, x_k, y_l, t^n)$ corresponds to the solution of the characteristics at time t (of the two dimensional system (2.6)) whose value at time t^n was the grid point (x_k, y_l). The cubic B-spline S is defined as follows

$$6S(x) = \begin{cases} (2 - |x|)^3 & \text{if } 1 \le |x| \le 2, \\ 4 - 6x^2 + 3|x|^3 & \text{if } 0 \le |x| \le 1, \\ 0 & \text{otherwise.} \end{cases}$$

In the expression (3.8), the weight $w^n_{k,l}$ is associated to the particle located at the grid point (x_k, y_l) at time t^n; it corresponds to the coefficient of the cubic spline determined by the following interpolation conditions

$$\begin{aligned} f(t^n, x_i, y_j) &= \sum_{k,l} \omega^n_{k,l} S(x_i - X_1(t^n; x_k, y_l, t^n)) S(y_j - X_2(t^n; x_k, y_l, t^n)) \\ &= \sum_{k,l} \omega^n_{k,l} S(x_i - x_k) S(y_j - y_l). \end{aligned}$$

Adding boundary conditions (for example the value of the normal derivative of f at the boundaries, we obtain a set of linear systems in each direction from which the weights $\omega^n_{k,l}$ can be computed as in [19, 12].

We can now express the full algorithm for the forward semi-Lagrangian method

- Step 0: Initialize $f^0_{i,j} = f_0(x_i, y_j)$
- Step 1: Compute the cubic splines coefficients $\omega^0_{k,l}$ such that

$$f^0_{i,j} = \sum_{k,l} \omega^0_{k,l} S(x_i - x_k) S(y_j - y_l),$$

- Step 2: Integrate (2.6) from t^n to t^{n+1}, given as initial data the grid points $X(t^n) = (x_k, y_l)$ to get $X(t; x_k, y_l, t^n)$ for $t \in [t^n, t^{n+1}]$, assuming the advection velocity U is known. We shall explain in the sequel how it is computed for our typical examples.
- Step 3: Project on the phase space grid using (3.8) with $t = t^{n+1}$ to get $f^{n+1}_{i,j} = f^{n+1}(x_i, y_j)$
- Step 4: Compute the cubic spline coefficients $\omega^{n+1}_{k,l}$ such that

$$f^{n+1}_{i,j} = \sum_{k,l} \omega^{n+1}_{k,l} S(x_i - x_k) S(y_j - y_l).$$

- Go to Step 2 for the next time step.

3.2 FSL: An explicit solution of the characteristics

For BSL, especially for the solution of the characteristics, it is possible to choose algorithms based on two time steps with field estimations at intermediate times. Generally, you have to use a fixed-point algorithm, a Newton-Raphson method (see [19]), a prediction correction one or also Taylor expansions (see [12]) in order to find the foot of the characteristics. This step of the global algorithm costs a lot (see [19]). It is no longer needed in FSL, where the starting point of the characteristics is known so that traditional methods to solve ODEs, like Runge-Kutta algorithms can be incorporated to achieve high order accuracy in time. Let us show the details of this explicit solution of the characteristics, in Vlasov-Poisson and Guiding-Center models.

In both cases, the dynamical system (2.6) has to be solved. With FSL, $X(t^n)$, $U(X(t^n), t^n)$ are known. You can choose your favorite way of solving this system on each time step, since the initial conditions are explicit. This leads to the knowledge of $X(t^{n+1})$ and $U(X(t^{n+1}), t^{n+1})$ so that Step 2 of the previous global algorithm is completed.

As examples of forward solvers for the characteristics curves, the second-order Verlet algorithm, Runge-Kutta 2 and Runge-Kutta 4 will be proposed for Vlasov-Poisson, and, as Verlet cannot be applied, only Runge-Kutta 2 and 4 will be used for the Guiding-Center model.

For Vlasov-Poisson, we denote by $X(t^n) = (X_1(t^n), X_2(t^n)) = (x^n, v^n)$ the mesh of the phase space, and $U(X(t^n), t^n) = (v^n, E(x^n, t^n))$ the advection velocity. The Verlet algorithm can be written

- Step 1: $\forall k, l,\ v^{n+\frac{1}{2}}_{k,l} - v^n_l = \frac{\Delta t}{2} E(x^n_k, t^n)$,
- Step 2: $\forall k, l,\ x^{n+1}_{k,l} - x^n_k = \Delta t\, v^{n+1/2}_{k,l}$,
- Step 3: compute the electric field at time t^{n+1}
  - deposition of the particles $x^{n+1}_{k,l}$ on the spatial grid x_i for the density ρ: $\rho(x_i, t^{n+1}) = \sum_{k,l} \omega^n_{k,l} S(x_i - x^{n+1}_{k,l})$, like in a PIC method.
  - solve the Poisson equation on the grid x_i: $E(x_i, t^{n+1})$.
- Step 4: $\forall k, l,\ v^{n+1}_{k,l} - v^{n+\frac{1}{2}}_{k,l} = \frac{\Delta t}{2} E(x^{n+1}_{k,l}, t^{n+1})$.

A second or fourth order Runge-Kutta algorithms can also be used to solve the characteristics curves of the Vlasov-Poisson system forward in time. The fourth order Runge-Kutta algorithm needs to compute intermediate values in time of the density and the electric field. Let us detail the algorithm omitting the indices k, l for the sake of simplicity

- Step 1: $k_1 = (v^n, E(x^n, t^n)) = (k_1(1), k_1(2))$,
- Step 2: compute the electric field at intermediate time t_1:
  - deposition of the particles on the spatial grid x_i for the density ρ: $\rho(x_i, t_1) = \sum_{k,l} \omega_{k,l}^n S[x_i - (x_k^n + \Delta t/2\ k_1(1))]$.
  - solve the Poisson equation on the grid x_i: $E(x_i, t_1)$.
- Step 3: compute $k_2 = (v^n + \frac{\Delta t}{2} k_1(2), E(x^n + \frac{\Delta t}{2} k_1(1), t_1)$
- Step 4: compute the electric field at intermediate time t_2:
  - deposition of the particles on the spatial grid x_i for the density ρ: $\rho(x_i, t_2) = \sum_{k,l} \omega_{k,l}^n S[x_i - (x_k^n + \Delta t/2\ k_2(1))]$.
  - solve the Poisson equation on the grid x_i: $E(x_i, t_2)$.
- Step 5: compute $k_3 = (v^n + \frac{\Delta t}{2} k_2(2), E(x^n + \frac{\Delta t}{2} k_2(1), t_2)$
- Step 6: compute the electric field at intermediate time t_3:
  - deposition of the particles on the spatial grid x_i for the density ρ: $\rho(x_i, t_3) = \sum_{k,l} \omega_{k,l}^n S[x_i - (x_k^n + \Delta t\ k_3(1))]$.
  - solve the Poisson equation on the grid x_i: $E(x_i, t_3)$.
- Step 7: compute $k_4 = (v^n + \Delta t\ k_3(2), E(x^n + \Delta t\ k_3(1), t_3)$
- Step 8: $X^{n+1} - X^n = \frac{\Delta t}{6} [k_1 + 2k_2 + 2k_3 + k_4]$

In both Verlet and Runge-Kutta algorithms, the value of E at intermediate time steps is needed (step 3 for Verlet and steps 3, 5 and 7 for Runge-Kutta 4). This is achieved as in PIC algorithms by advancing the particles (which coincide at time t^n with the mesh in this method) up to the required intermediate time. Using a deposition step, the density is computed thanks to cubic splines of coefficients w_i^n on the mesh at the right time, and thus the electric field can also be computed at the same time thanks to the Poisson equation. Using an interpolation operator, the electric field is then evaluated at the required location (in steps $3, 5$ and 7). Let us remark that this step involves a high order interpolation operator (cubic spline for example) which has been proved in our experiments to be more accurate than a linear interpolation (see section 4).

For the Guiding-Center equation, the explicit Euler method, and also Runge-Kutta type methods (of order 2, 3 and 4) have been implemented. There is no technical difficulty with computing high order methods. This is one of the general interests of forward methods. The time algorithm for solving the characteristics at the fourth order is similar to those presented in the Vlasov-Poisson case. However, there is a additional difficulty in the deposition step which enables to evaluate the density at intermediate time steps; indeed, the deposition is two-dimensional since the unknown does not depend on the velocity variable in this case.

Let us summarize the main steps of the second order Runge-Kutta method applied to the guiding center model of variables $X^n = (x^n, y^n)$ and of advection field $U(X^n, t^n) = E^\perp(X^n, t^n)$

- Step 1: $\tilde{X}^{n+1} - X^n = \Delta t E^\perp(X^n, t^n)$
- Step 2: Compute the electric field at time t^{n+1}
  - two-dimensional deposition of the particles on the spatial grid (x_j, y_i) for the density ρ: $\rho(x_j, y_i, t^{n+1}) = \sum_k \omega_k^n S[x_j - x_{k,l}^{n+1}] S[y_i - y_{k,l}^{n+1}]$
  - solve the two-dimensional Poisson equation on the grid x_j: $E(x_j, y_i, t_{n+1})$.
- Step 3: $X^{n+1} - X^n = \frac{\Delta t}{2} \left[E^\perp(X^n, t^n) + E^\perp(\tilde{X}^{n+1}, t^{n+1}) \right]$

Here, the numerical solution of the two-dimensional Poisson's equation is based on Fourier transform coupled with finite difference method. See details in Appendix II.

3.3 FSL - BSL Cubic Spline Interpolation

We are going to compare how spline coefficients are computed recurrently, for one dimensional transport problems, for the sake of simplicity.

FSL: deposition principle On our mesh, the grid points $x_i = i\Delta x, i = 0, .., N_x$ at a time n can be regarded as particles. We have a distribution function which is projected onto a cubic splines basis. Thus, we know $f(t^n, x)$, $\forall x$, then the particles move forward, and we have to compute $f(t^{n+1}, x_i)$, $i = 0, ..., N_x$, reminding that f is constant along the characteristics, and that the particles follow characteristics between t^n and t^{n+1}.

In fact, to each mesh point x_i, a spline coefficient ω_k is linked. The thing to understand, is that these coefficients are transported up to the deposition phase. The key is then to compute them recurrently as follows:

- Deposition step

$$\begin{aligned} f^{n+1}(x_i) &= \sum_k \omega_k^n S(x_i - X(t^{n+1}; x_k, t^n)) \\ &= \sum_{k/X(t^{n+1};x_k,t^n)\in[x_{i-1},x_{i+2}]} \omega_k^n S(x_i - X(t^{n+1}; x_k, t^n)), \end{aligned}$$

- Update of the splines coefficients ω_k^{n+1} using the interpolation conditions

$$f^{n+1}(x_i) = \sum_{k=i-1}^{i+2} \omega_k^{n+1} S(x_i - x_k),$$

The number of points which actually take part in the new value of $f^{n+1}(x_i)$ (here 4) is directly linked with the spline degree you choose. A p-Spline for example has a $(p+1)$ points support.

In a 1D way of regarding the problem, you can easily prove the mass conservation:

$$\begin{aligned} m^{n+1} &= \Delta x \sum_i f^{n+1}(x_i) \\ &= \Delta x \sum_i \sum_k \omega_k^n S(x_i - X(t^{n+1}; x_k, t^n)) \\ &= \Delta x \sum_k \omega_k^n = \Delta x \sum_i f^n(x_i) = m^n. \end{aligned}$$

Merely with the spline property of unit partition $\sum_i S(x - x_i) = 1$ for all x.

BSL: interpolation principle Let us introduce some notations. The foot of the characteristics $X(t^n, x_i, t^{n+1})$ belongs to the interval $[x_l, x_{l+1}[$. Then the reconstructed distribution function can be written

- Interpolation step

$$\begin{aligned} f^{n+1}(x_i) &= f^n(X(t^n; x_i, t^{n+1})) \\ &= \sum_{k=l-1}^{l+2} \omega_k^n S(X(t^n; x_i, t^{n+1}) - x_k) \end{aligned}$$

- Update of the splines coefficients ω_k^{n+1} using the interpolation conditions

$$f^{n+1}(x_i) = \sum_{k=i-1}^{i+2} \omega_k^{n+1} S(x_i - x_k)$$

Figure 1: Principle of FSL (left) and BSL (right) for linear splines.

Here, we denoted by $X(t^n; x_i, t^{n+1})$ the foot of the characteristic coming from x_i. The reader is referred to [19, 12] for more details on BSL interpolation.

In both cases, a linear system has to be solved, of equivalent complexity, so our method is as efficient at this level as BSL is.

3.4 Basic differences between FSL and BSL

Let us now explain the basic differences between forward and backward semi-Lagrangian methods. In both cases, a finite set of mesh points $(x_m)_{m=1..N}$ is used, and the values of the function f at the mesh points at a given time step t^n are considered. The aim is to find the new values of f on the grid at the next time step t^{n+1}.

BSL For BSL, in order to find the $(n+1)$-th value of f at x_m, we follow the characteristic curve which goes through x_m, backward in time, until time t^n. The arrival point will be called the foot of the characteristics and does not necessarily coincide with a mesh point. Hence, we use any interpolation technique to compute f at this point, knowing all the values of the mesh at this time. This leads to the new value of $f(x_m)$. Let us summarize:

- find the foot of the characteristics $X(t^n)$ knowing $X(t^{n+1}) = x_m$ (mesh point)
- interpolate using the grid function which is known at time t^n.

FSL For FSL, the principle is quite different. The characteristics beginning at time t^n on the grid points are followed, during one time step, and the end of the characteristics (*i.e.* at time t^{n+1}) is found. At this moment, the known value is deposited to the nearest grid points (depending on the chosen method). This deposition step is also performed in PIC codes on the spatial grid only, in order to get the sources for the computation of the electromagnetic field. Once every grid points has been followed, the new value of f is obtained by summing all contributions. The FSL method can be summarized as follows

- find the end of the characteristics $X(t^{n+1})$ leaving from $X(t^n) = x_m$ (mesh point)
- deposit on the grid and compute the new particle weights.

4 Numerical results

This section is devoted to the numerical implementation of the forward semi-Lagrangian method. In particular, comparisons with the backward semi-Lagrangian method will be performed to validate the new approach.

4.1 Hill's equation

In order to check that high orders are really reached, a particularly easy model can be used, in which there are no self-consistent fields. This leads to a 1D model with an external force field written $-a(t)x$, where a is a given periodical function. The Vlasov equation becomes:

$$\frac{\partial f}{\partial t} + v\partial_x f - a(t)x\partial_v f = 0, \tag{4.9}$$

The solution of this equation is seen through its characteristics, solutions of

$$\frac{dX}{dt} = V, \qquad \frac{dV}{dt} = -a(t)X \tag{4.10}$$

thus, X is solution of Hill's equation:

$$\frac{d^2X}{dt^2} + a(t)X = 0 \tag{4.11}$$

Let's note that this equation can be written in a general way $\frac{du}{dt} = A(t)u$, where A is a matrix valued periodic function. Since this is a 2D linear system, its solution is a 2D vector space and it is sufficient to find two independent solutions.

Let ω, $\psi \in C^2(\mathbb{R}^+, \mathbb{R})$, with $\omega(t) > 0 \ \ \forall t \in \mathbb{R}^+$, so that ω is solution of the differential equation

$$\frac{d^2\omega}{dt^2} + a(t)\omega - \frac{1}{\omega^3} = 0 \quad \frac{d\psi}{dt} = \frac{1}{\omega^2} \tag{4.12}$$

So $u(t) = \omega(t)e^{i\psi(t)}$ and $v(t) = \omega(t)e^{-i\psi(t)}$ are two independent solutions of Hill's equation (see [13] for more details) which can be determined numerically.

For this test case, the initial distribution function will be:

$$f_0(x,v) = e^{-\frac{x^2}{2\omega^2} - \frac{\omega^2 v^2}{2}}, \forall (x,v) \in [-12,12]^2.$$

The associated solution $f(x,v,t)$ will depend only on $A\omega(t)$. In particular, f will have the same periodicity as a and ω. This is what will be used for testing the code. For different orders (2 and 4), and different Δt, $x_{rms}(t) = \sqrt{\int x^2 f(x,v,t)dxdv}$ will be displayed on Fig 2. This function should be periodic, and thus should reach the same test value $x_{rms}(0)$ at each period. The error will be measured between the ten first computed values and the exact one, for the ten first periods. Then these errors will be summed, so that a L^1 norm of the error is dealt with:

$$err = \sum_{k=0}^{k=10} e_k, \quad \text{with} \quad e_k = |x_{rms}(2k\pi) - x_{rms}(0)|.$$

The order of the method is checked in Figure 2. Note that $N_x = N_v = 1024$ to make sure that convergence is achieved for the interpolation step. The expected order is achieved for a certain Δt interval. If Δt becomes too small, a kind of saturation happens. This is due to the term in $\frac{h^{m+1}}{\Delta t}$ (where $h = \Delta x = \Delta v$) in the theoretical estimation of the error for backward methods ([2]), which becomes too high and prevents us from keeping the correct order. A forthcoming paper will try to do the same kind of error estimation for the forward method.

4.2 Vlasov-Poisson case

Landau damping The initial condition associated to the scaled Vlasov-Poisson equation (2.1)-(2.2) has the following form

$$f_0(x,v) = \frac{1}{\sqrt{2\pi}} \exp(-v^2/2)(1 + \alpha\cos(kx)), \quad (x,v) \in [0, 2\pi/k] \times \mathbb{R}, \tag{4.13}$$

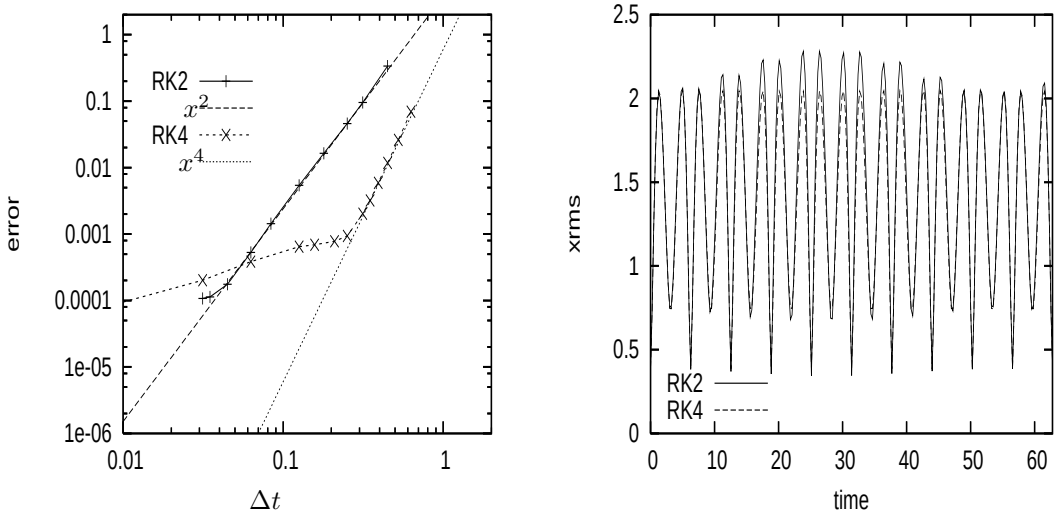

Figure 2: Error as a function of Δt for RK2 and RK4 (left) and x_{rms} as a function of time, for $\Delta t = 2\pi/25$, RK2 and RK4 (right).

where $k = 0.5$ is the wave number and $\alpha = 0.001$ is the amplitude of the perturbation, so that linear regimes are considered here. A cartesian mesh is used to represent the phase space with a computational domain $[0, 2\pi/k] \times [-v_{max}, v_{max}]$, $v_{max} = 6$. The number of mesh points in the spatial and velocity directions is designated by $N_x = 64$ and $N_v = 64$ respectively. Finally, the time step is equal to $\Delta t = 0.1$ and the Verlet algorithm is used to compute the characteristics.

In this context, it is possible to find an exact value of the dominant mode solution of the linearized Vlasov-Poisson equation (see Appendix I for some details). The exact electric field corresponding to the dominant mode reads

$$E(x,t) = 4\alpha \times 0.3677 e^{-0.1533t} \sin(0.5x) \cos(1.4156t - 0.5326245).$$

On Fig. 3, the analytical solution of the L^2 norm of the electric field and the implemented one are plotted. It can be observed that the two curves are very close to each other. In particular, the damping rate and the frequency of the wave are well recovered ($\gamma = -0.1533$ and $\omega = 1.4156$) by the method. Similar precision is achieved for different values of k leading to different value of the damping rate and of the frequency (see Fig. 3).

The recurrence effect that occurs with the present velocity discretization on a uniform grid, at $T_R \approx 80\,\omega_p^{-1}$ can also be remarked. This value is in good agreement with the theoretical recurrence time which can be predicted in the free-streaming case (see [15]) $T_R = \frac{2\pi}{k\Delta v}$.

This test case has also been solved with the "hybrid" method in which the deposition step is only performed every T time steps. In all other steps, the remapping (or deposition) step is not performed, therefore, it can be linked with a PIC method. As it was already said, it is not really a PIC method since the spline coefficients are different on the phase space grid and are updated at each remapping step, whereas in classical PIC methods, these coefficients (called *weights*) are constant equal to $\frac{n_0}{N_{part}}$ where N_{part} is the number of particles. On Fig. 4, the electric field is plotted again, for different values of T, and $\Delta t = 0.1$, with $N_x = N_v = 128$ points. As expected, the method works well, even for large values of T. Only a kind of saturation can be observed, and it can be seen that values smaller than 2^{-18} are not well treated, because of the lack of accuracy of the hybrid method. Nevertheless, the results are convincing: the computation gets faster as T gets larger, and a good accuracy is still reached.

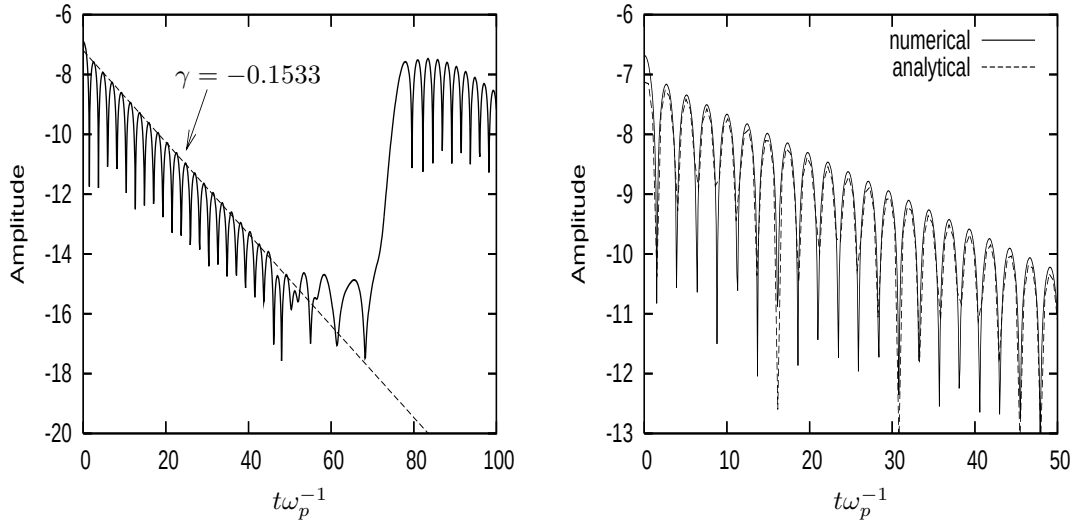

Figure 3: Linear Landau damping for $k = 0.5$ (left) and $k = 0.4$ (right)

Two stream instability This test case simulates two beams with opposit velocities that encounter (see [9, 15]). The corresponding initial condition can be given by

$$f_0(x, v) = \mathcal{M}(v)v^2[1 - \alpha\cos(kx)],$$

with $k = 0.5$ and $\alpha = 0.05$. The computational domain is $[0, 2\pi/k] \times [-9, 9]$ which is sampled by $N_x = N_v = 128$ points. The Verlet algorithm is used to compute the characteristics with $\Delta t = 0.5$.

We are interested in the following diagnostics: the first three modes of the electric field, the electric energy $1/2\|E(t)\|^2_{L^2}$ and the time evolution of the phase space distribution function.

On Fig. 5, we plot the time history of the first three Fourier modes of the electric field: $|E_1|, |E_2|, |E_3|$ denotes the amplitudes of $\hat{E}(k = 0.5)$, $\hat{E}(k = 1)$ and $\hat{E}(k = 1.5)$ respectively. We observe that after an initial phase, the first mode exponentially increases to reach its maximum at $T \approx 18\,\omega_p^{-1}$. After this phase and until the end of the simulation, a periodic behavior is observed which translates the oscillation of the trapped particles in the electric field; in particular, a vortex rotates with a period of about $18\,\omega_p^{-1}$. The other modes $|E_2|$ and $|E_3|$ also grow exponentially and oscillate after the saturation. However, their amplitude remains inferior to that of the first mode. Similar observations can be performed for the electric energy which reaches its maximum at $T \approx 18\,\omega_p^{-1}$ after an important and fast increase (from $t = 8$ to $t = 18\,\omega_p^{-1}$).

This test case was also solved with the hybrid method to test the capability in the nonlinear regime. On Fig. 6, the first Fourier mode of the electric field is displayed for different T, with $\Delta t = 0.5$, and 128 points in each direction. It can be observed that during the first phase, which is a linear one, even for big T, the results are quite accurate for all values of T. The hybrid method seems to have more difficulty after this linear phase. Numerical noise, one of the main drawbacks of PIC methods can be observed as T gets higher. The phenomenon can be understood looking at the distribution function. On Fig. 6 the noise clearly appears on f. Noisy values quickly reach high values which prevent the method from being accurate enough. They are more important in our hybrid method than in classical PIC ones, because of the deposition step, where the particles weight play their role. Indeed, if particles with very different weights are located at the same place, the deposition does not take into account properly the particles of low weights compared to those of heavy weights. On Fig. 6, it can be seen that the vortex which appears at the middle of the distribution and should stay there slowly leaves out of the domain. This can be explained as a kind of diffusion. Nevertheless, if T remains very little $(2-4)$, the results are really good. It can also be noticed that Δt plays an important role, actually, when a smaller Δt is chosen, the results remain good for bigger T. As an example, if $\Delta t = 0.1$, results remain acceptable until $T = 16$.

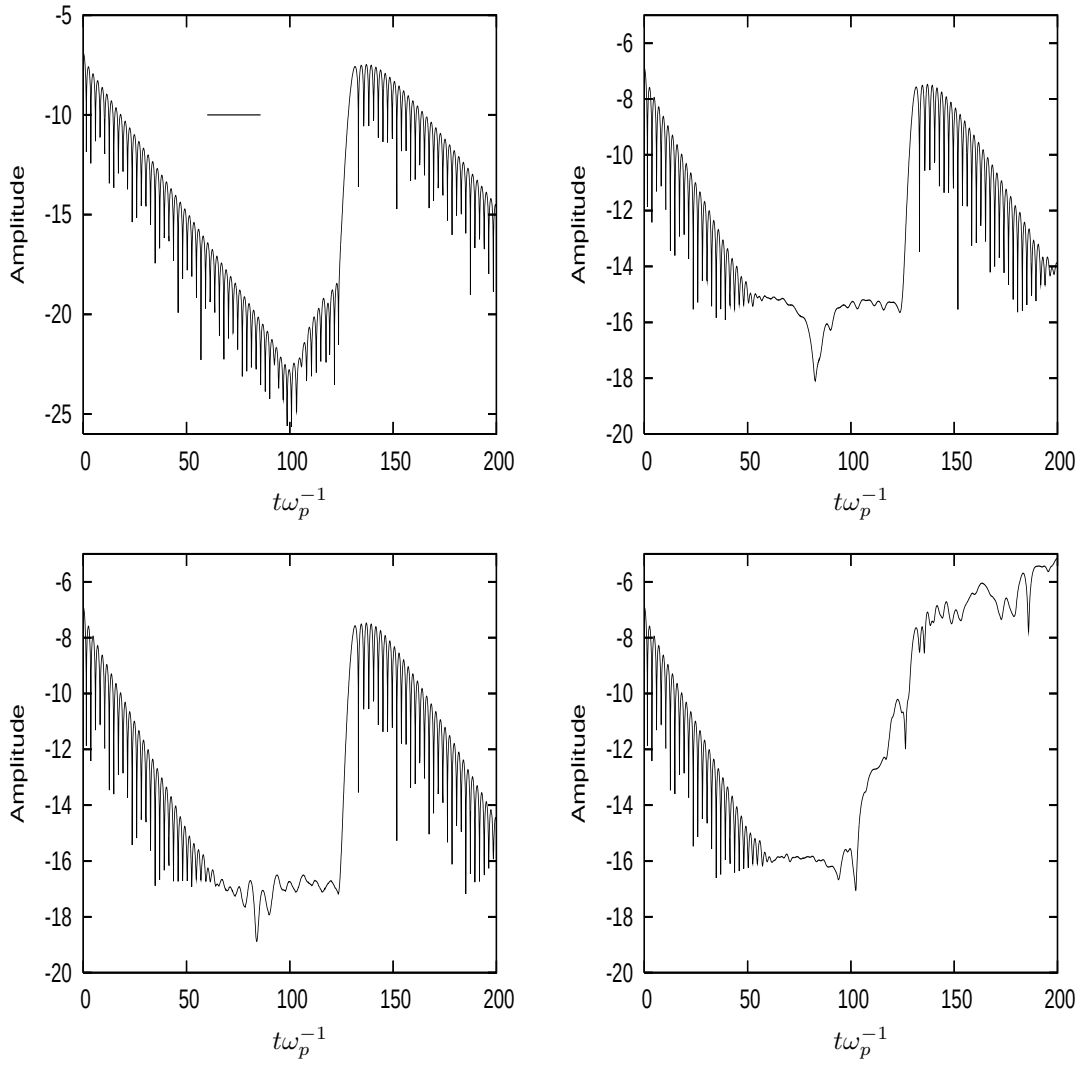

Figure 4: Linear Landau damping for $k = 0.5$ and for different number of T: from up to down and left to right: $T = 1, T = 2, T = 16, T = 256$.

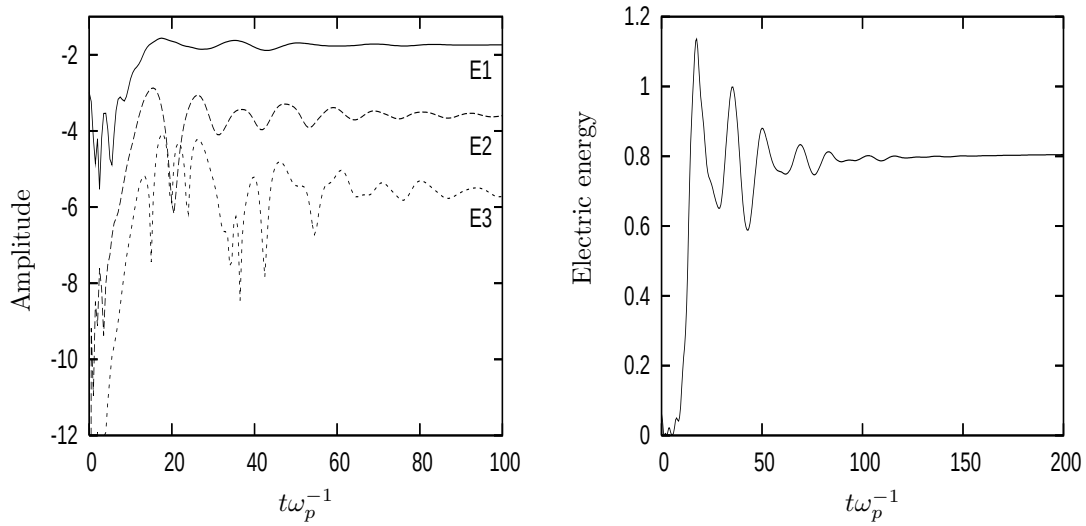

Figure 5: Two stream instability: Time evolution of the three first modes of the electric field (left) and of the electric energy (right).

Bump on tail Next, we can apply the scheme to the bump-on-tail instability test case for which the initial condition writes

$$f_0(x,v) = \tilde{f}(v)[1+\alpha\cos(kx)],$$

with

$$\tilde{f}(v) = n_p \exp(-v^2/2) + n_b \exp\left(-\frac{|v-u|^2}{2v_t^2}\right)$$

on the interval $[0, 20\pi]$, with periodic conditions in space. The initial condition f_0 is a Maxwellian distribution function which has a bump on the Maxwell distribution tail; the parameters of this bump are the following

$$n_p = \frac{9}{10(2\pi)^{1/2}}, n_b = \frac{2}{10(2\pi)^{1/2}}, u = 4.5, v_t = 0.5,$$

whereas the numerical parameters are $N_x = 128, N_v = 128, v_{max} = 9, \Delta t = 0.5$. The Runge-Kutta 4 algorithm is used to compute the characteristics.

We are interested in the time evolution of the spatially integrated distribution function

$$F(t,v) = \int_0^{20\pi} f(t,x,v)dx,$$

and in the time history of the electric energy $1/2\|E(t)\|_{L^2}^2$. For this latter diagnostic, we expect oscillatory behavior of period equal to 1.05; moreover, since an instability will be declared, the electric energy has to increase up to saturation at $t \approx 20.95$ and to converge for large times to 36% of its highest value (see [15, 17]).

On Figures 7 and 8, we plot the electric energy as a function of time. We can observe that oscillations appear, the period of which can be evaluated to 1.; then the maximum value is reached at $t \approx 21$ and the corresponding amplitude is about 9, which is in very good agreement with the results presented in [15]. Then the amplitude of the electric energy decreases and presents a slower oscillation due to the particle trapping. Finally, it converges to an amplitude of about 2.8 which is very close to the predicted value. However, for very large times (at $t = 250\,\omega_p^{-1}$), FSL using lower time integrator algorithms (Runge-Kutta 2 or Verlet algorithms) leads to bad results (see Fig. 8). A very precise computation of the characteristics is required for this test and the use of Runge-Kutta 4 is crucial. The results obtained by BSL (see Fig. 7) are very close to those obtained by FSL using Runge-Kutta 4. Moreover, if Δt increases (up to $\Delta t \approx 0.75$), BSL presents some unstable results whereas FSL remains stable up to $\Delta t \approx 1$. The use of high order time integrators

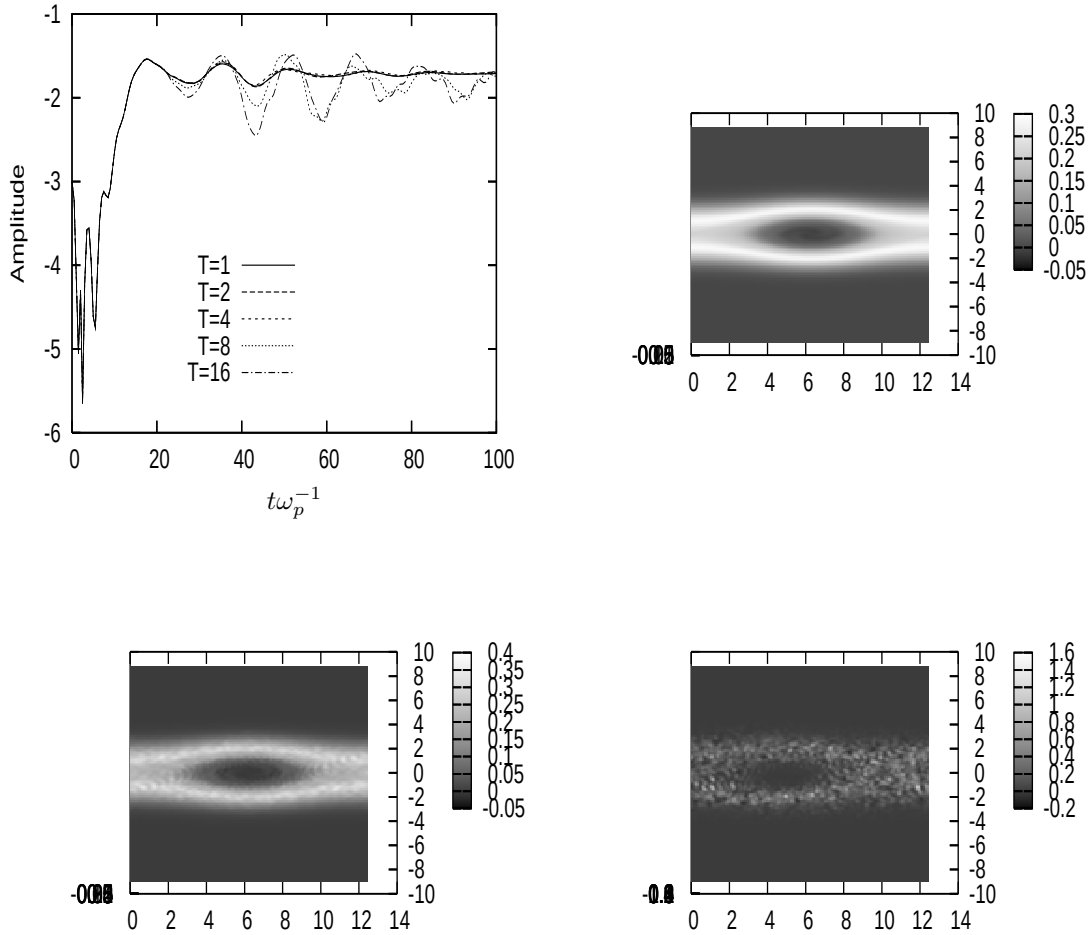

Figure 6: Two stream instability: Time evolution of the first mode of the electric field (up and left) and distribution function at time $t = 100\,\omega_p^{-1}$ for $T = 1, 4, 8$.

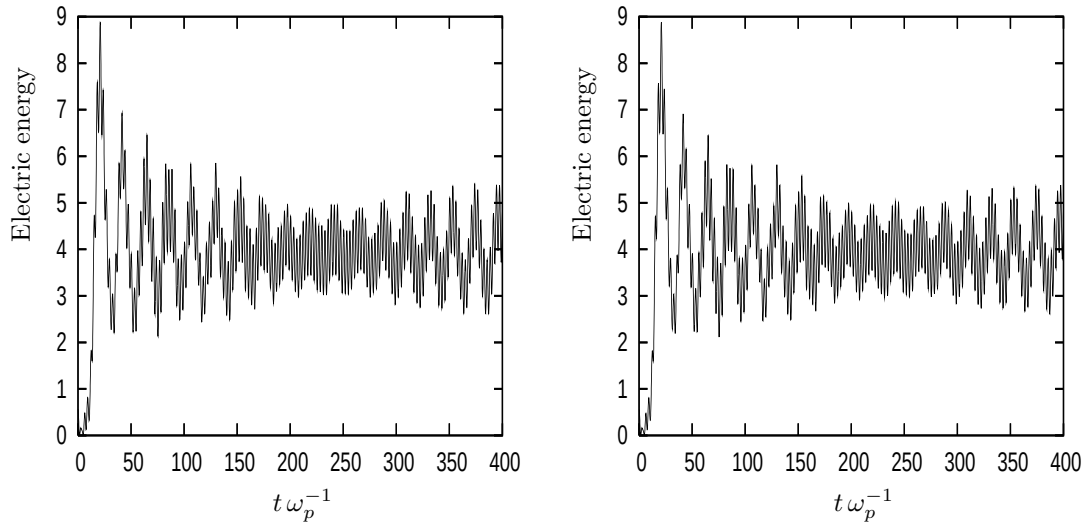

Figure 7: Bump on tail instability: time evolution of the electric energy for FSL (left) and BSL (right).

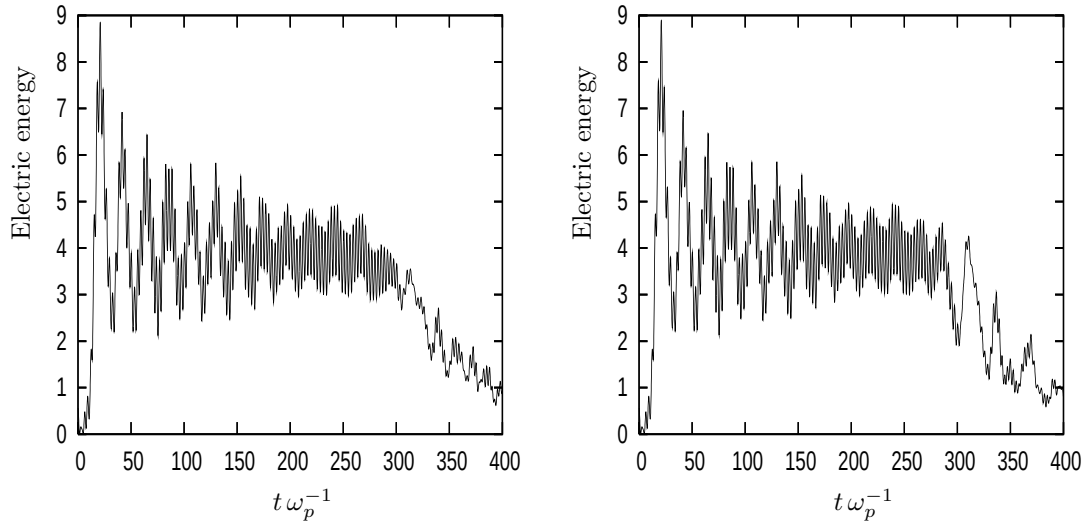

Figure 8: Bump on tail instability: time evolution of the electric energy for FSL RK2 (left) and FSL Verlet (right).

leads to an increase of accuracy but also to more stable results as Δt increases. It has been remarked that linear interpolation of the electric field is not sufficient to obtain accurate results with FSL-Runge-Kutta 4 and cubic spline are used to that purpose.

Fig. 9 and Fig. 10 shows the time development of the spatially integrated distribution function for FSL and BSL. We observe that very fast, the bump begins to be merged by the Maxwellian and a plateau is then formed at $t \approx 30 - 40\,\omega_p^{-1}$.

4.3 Guiding-center case

Kelvin-Helmoltz instability In order to validate our guiding-center code, we used two test cases introduced in [17] and [11].

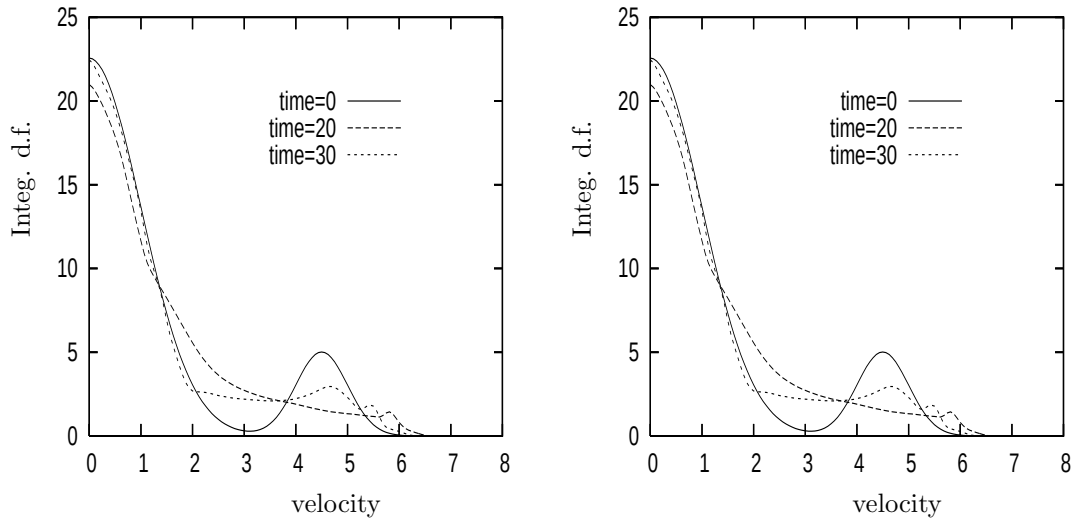

Figure 9: Bump on tail instability: time development of the spatially integrated distribution function for FSL (left) and BSL (right).

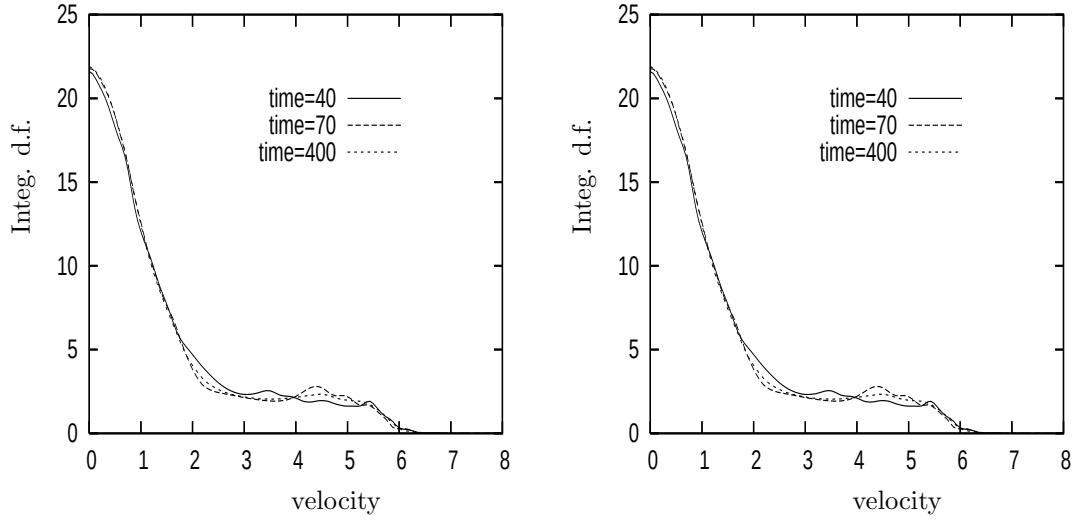

Figure 10: Bump on tail instability: time development of the spatially integrated distribution function for FSL (left) and BSL (right).

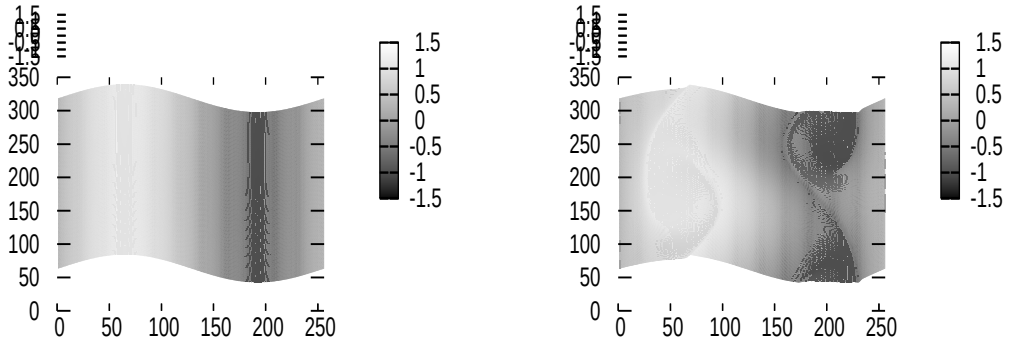

Figure 11: Kelvin Helmholtz instability 1: distribution function at time $t = 0,30\,\omega_p^{-1}$

4.3.1 First test case

The corresponding initial condition is

$$\rho(x,y,t=0) = \rho^0(y) + \epsilon\rho^1(y)$$

coupled with Poisson's equation:

$$\phi = \phi^0(y) + \epsilon\phi^1(y)\cos(kx)$$

The instability is created choosing an appropriate ρ^1 which will perturb the solution around the equilibrium one (ρ^0, ϕ^0). Using the the work of Shoucri, we will take:

$$\rho(x,y,t=0) = \sin(y) + 0.015\sin(\frac{y}{2})\cos(kx)$$

where $k = \frac{2\pi}{L_x}$ and L_x the length of the domain in the x-direction

The numerical parameters are:

$$N_x = N_y = 128, \Delta t = 0.5.$$

The domain size has an impact on the solution. The interval $[0, 2\pi]$ will be used on the y-direction, and respectively $L_x = 7$ and $L_x = 10$. This leads to real different configurations:

With $L_x = 7$, Shoucri proved that the stable case should be dealt with. That is what was observed with this code.

With $L_x = 10$, the unstable case is faced. The results prove it on figure Fig. 11 and 12.

For this test case, the evolution of the energy $\int E^2 dxdy$ and enstrophy $\int \rho^2 dxdy$ will also be plotted on Fig. 13. These should be theoretically invariants of the system. Like for other semi-Lagrangian methods, the energy lowers during the first phase, which is the smoothing one, where micro-structures can not be solved properly. Nevertheless, the energy is well conserved. Moreover, on Fig. 13, FSL using second and fourth order Runge-Kutta's methods are compared to the BSL method. As observed in the bump-on-tail test, the Runge-Kutta 4 leads to more accurate results and is then very close to BSL. However, BSL seems to present slightly better behavior compared to FSL-Runge-Kutta 4. But FSL-Runge-Kutta 4 enables to simulate such complex problems using higher values of Δt (see Fig. 14). We observed for example that the use of $\Delta t = 1$ gives rise to very reasonable results since the L^2 norm of the electric field E decreases of about $4\,\%$. Let us remark that BSL becomes unstable for $\Delta t \geq 0.7$.

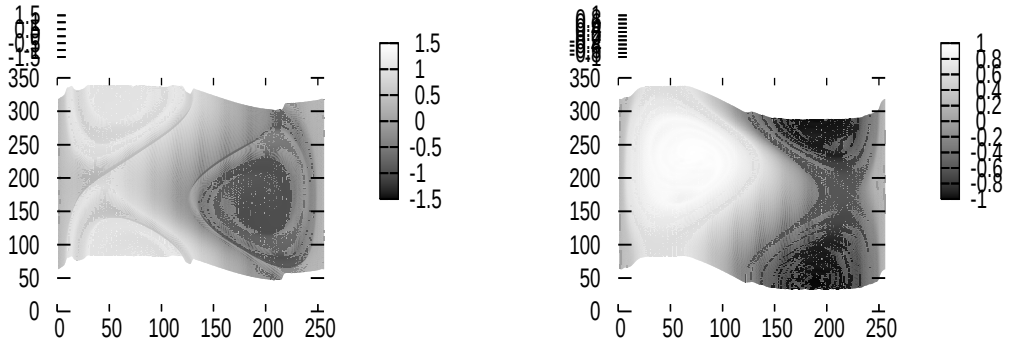

Figure 12: Kelvin Helmholtz instability 1: distribution function at time $t = 50,500\,\omega_p^{-1}$

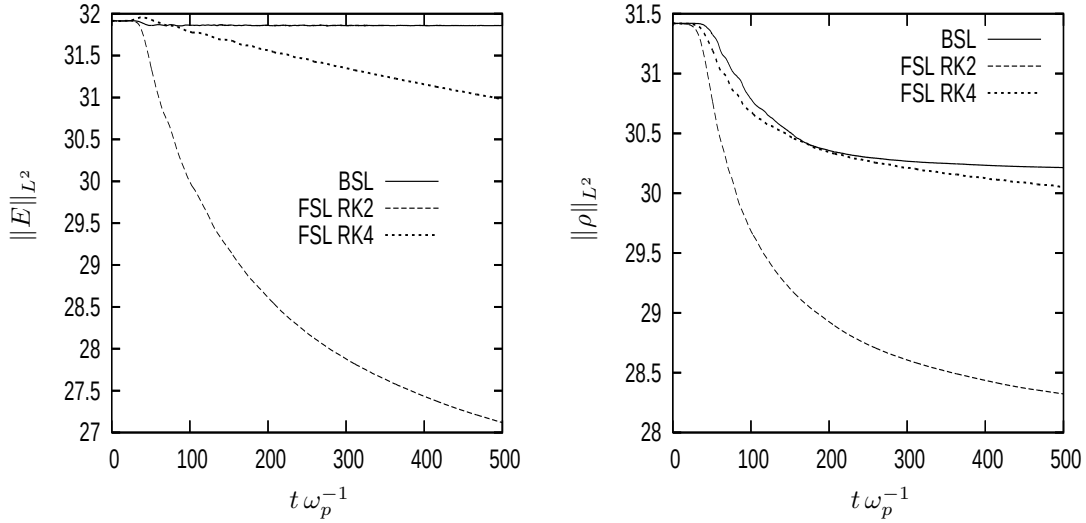

Figure 13: Kelvin Helmholtz instability 1: time history of L^2 norms of E (left) and of ρ (right). Comparison between FSL and BSL.

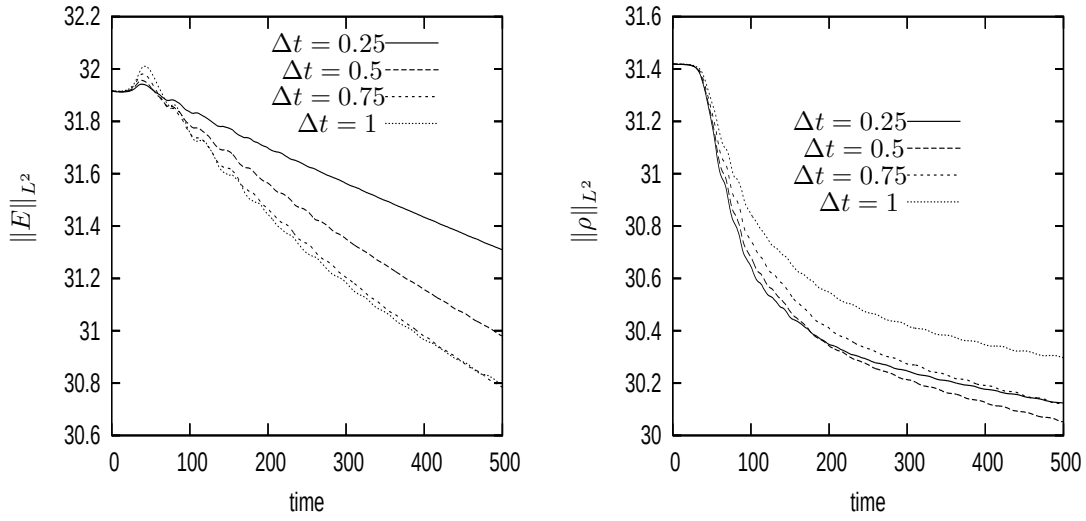

Figure 14: Kelvin Helmholtz instability 1: time history of L^2 norms of E (left) and of ρ (right). Comparison of the results for RK4 for different values of Δt.

5 Conclusion and perspectives

In this paper, we introduced the forward semi-Lagrangian method for Vlasov equations. The method has been tested on two different models, the one-dimensional Vlasov-Poisson one, and the guiding-center one. Different test cases have been simulated, and they are quite satisfying. The results are in some cases a bit less accurate, with respect to the conservation of invariants, than with the classical BSL method, but enables the use of very large time steps without being unstable and recovering all the expected aims. No iterative methods anymore, and high order time schemes can be use in a straightforward manner. The next step will be to test the method with the Vlasov-Maxwell model, in which we will try to solve properly the charge conservation problem, which is the ultimate goal. We will try to use PIC results about that conservation, for example in [1]. We will also try to prove theoretically the convergence of this method.

6 Appendix I: Linearized Vlasov Poisson and Landau damping

In classical plasma physics textbooks, only the dispersion relations are computed for the linearized Vlasov-Poisson equation. However using the Fourier and Laplace transforms as for the computation of the dispersion relation and inverting them, it is straightforward to obtain an exact expression for each mode of the electric field (and also the distribution function if needed). Note that each mode corresponds to a zero of the dispersion relation.

The solution of the Landau damping problem is obtained by solving the linearized Vlasov-Poisson equation with a perturbation around a Maxwellian equilibrium, which corresponds to the initial condition $f_0(x,v) = (1+\epsilon\cos(kx))/\sqrt{2\pi}e^{-v^2/2}$. Let us introduce the plasma dispersion function Z of Fried and Conte [10]

$$Z(\eta) = \sqrt{\pi}e^{-\eta^2}[i - erfi(\eta)], \quad \text{where } erfi(\eta) = \frac{2}{\pi}\int_0^\eta e^{t^2}dt.$$

We also have, $Z'(\eta) = -2(\eta Z(\eta)+1)$. Then, denoting by $\widehat{E}(k,t)$ the Fourier transform of E and by $\widetilde{E}(k,\omega)$ the Laplace transform of $\widehat{E}$, the electric field, solution of linearized Vlasov-Poisson satisfies:

$$\widehat{E}(k,t) = \sum_j Res_{\omega=\omega_j}\widetilde{E}(k,\omega)e^{-i\omega t}$$

where

$$\widetilde{E}(k,\omega) = \frac{N(k,\omega)}{D(k,\omega)}$$

$$D(k,\omega) = 1 - \frac{1}{2k^2} Z'(\frac{\omega}{\sqrt{2}k}), \quad N(k,\omega) = \frac{i}{2\sqrt{2}k^2} Z(\frac{\omega}{\sqrt{2}k})$$

The dispersion relation corresponds to

$$D(k,\omega) = 0.$$

For each fixed k, this equation has different roots ω_j, and to which are associated the residues defining $\widehat{E}(k,t)$ that can be computed with Maple. These residues that in fact the values

$$\frac{N(k,\omega_j)}{\frac{\partial D}{\partial \omega}(k,\omega)}. \tag{6.14}$$

Let us denote by $\omega_r = Re(\omega_j)$, $\omega_i = Im(\omega_j)$, r will be the amplitude of (6.14) and φ its phase.

Remark: For each root $\omega = \omega_r + i\omega_i$, linked to $re^{i\varphi}$, there is another: $-\omega_r + i\omega_i$ linked to $re^{-i\varphi}$. Then keeping only the roots in which ω_i is the largest, which are the dominating ones after a short time, we get:

$$\widehat{E}(k,t) \approx re^{i\varphi} e^{-i(\omega_r + i\omega_i)t} + re^{-i\varphi} e^{-i(-\omega_r + i\omega_i)t} = 2re^{\omega_i t}\cos(\omega_r t - \varphi)$$

Taking the inverse Fourier transform, we finally get an analytical expression for the dominating mode of the electric field, which we use to benchmark our numerical solution:

$$E(x,t) \approx 4\epsilon r e^{\omega_i t}\sin(kx)\cos(\omega_r t - \varphi)$$

Remark This is not the exact solution, because we have kept only the highest Laplace mode. Nevertheless, after about one period in time, this is an excellent approximation of E, because the other modes decay very fast.

7 Appendix II: Solution of Poisson in the Guided Center model

7.1 Find ϕ

We have to solve:

$$-\Delta\phi(x,y) = \rho(x,y)$$

We use a Fourier transform in the x direction. This leads, for $i \in [1, N_x]$:

$$\frac{\partial^2 \widehat{\phi_i}(y)}{\partial y^2} = \xi^2 \widehat{\phi_i}(y) + \widehat{\rho_i}(y)$$

Let us introduce a notation. Thanks to Taylor Young formula, we have:

$$\delta u_i = \frac{u_{i+1} - 2u_i + u_{i-1}}{\Delta y^2} = \left(1 + \frac{\Delta y^2}{12}\frac{\partial^2}{\partial y^2}\right)\frac{\partial^2 u_i}{\partial y^2} + \mathcal{O}(\Delta_y^2).$$

Let us apply this to $\widehat{\phi_i}$

$$\delta\widehat{\phi_i} = \left(1 + \frac{\Delta y^2}{12}\frac{\partial^2}{\partial y^2}\right)(\xi^2\widehat{\phi_i} + \widehat{\rho_i}) + \mathcal{O}(\Delta_y^2) = \xi^2\widehat{\phi_i} + \widehat{\rho_i} + \frac{\Delta y^2}{12}(\xi^2\delta\widehat{\phi_i} + \delta\widehat{\rho_i}) + \mathcal{O}(\Delta_y^2).$$

Now, factorizing all of it, we get:

$$\widehat{\phi_{i+1}}\left(1 - \frac{\xi^2\Delta_y^2}{12}\right) + \widehat{\phi_i}\left(-2 + \frac{10\xi^2\Delta_y^2}{12}\right) + \widehat{\phi_{i-1}}\left(1 - \frac{\xi^2\Delta_y^2}{12}\right) = \Delta y^2(\widehat{\rho_{i+1}} + 10\widehat{\rho_i} + \widehat{\rho_{i-1}}) + \mathcal{O}(\Delta_y^4).$$

This is nothing but the solution of a linear system

$$A\widehat{\phi} = R,$$

where A is a tridiagonal and symmetric matrix and R is a modified right hand side which allows to achieve a fourth order approximation.

7.2 Find E

To compute the electric field from the electric potential, we have to solve $E = -\nabla\phi$. To achieve this task, a quadrature formula is used.

In the x direction, which is the periodic one, a third order Simpson method is used

$$\int_{x_{i-1}}^{x_{i+1}} E(x,y)dx = -\phi(x_{i+1},y) + \phi(x_{i-1},y) \approx \frac{1}{6}E_{i-1}(y) + \frac{1}{6}E_{i+1}(y) + \frac{2}{3}E_i(y)$$

where the $(\phi_i)_i$ is given by previous step. There is no problem with extreme values, since the system is periodic. We then find the values of the electric field E solving another tridiagonal linear system.

Whereas on the y-direction, Dirichlet conditions are imposed at the boundary. So, we can use the same strategy within the domain, but not on the two boundary points. Since we have a third order solution everywhere, we want to have the same order there, therefore we cannot be satisfied with a midpoint quadrature rule which is of second order. So we will add corrective terms, in order to gain one order accuracy. Here is how we do this.

$$\int_{y_0}^{y_1} E(x,y)dy = -\phi(x,1) + \phi(x,0) \approx \frac{dy}{2}(E(x,0) + E(x,1)) - \frac{dy^2}{12}(\rho(x,1) - \rho(x,0)) + f_\phi$$

where

$$f_\phi = \mathbb{F}_y^{-1}\left(\frac{\Delta_y^2}{12}\xi^2(\widehat{\phi(\xi,1)} - \widehat{\phi(\xi,0)})\right) = \frac{\Delta_y^2}{12}\left[-\partial_{xx}(\phi(x,1) - \phi(x,0))\right].$$

We want to find the precision of this method, thus, we would like to evaluate the following difference which is denoted by A:

$$A = \phi(x,0) - \phi(x,1) - \frac{dy}{2}(E(x,0) + E(x,1)) + \frac{dy^2}{12}(\rho(x,1) - \rho(x,0)) - f_\phi.$$

Using the Poisson equation and Taylor expansion, we have

$$\begin{aligned} A + E(x,0) + E(x,1) &= -\frac{2}{dy}(\phi(x,1) - \phi(x,0)) + \frac{dy}{6}(\rho(x,1) - \rho(x,0)) + \frac{dy}{6}(\partial_{xx}(\phi(x,1) - \phi(x,0)) \\ &= -\frac{2}{dy}(\phi(x,1) - \phi(x,0)) - \frac{dy}{6}(\partial_{yy}(\phi(x,1) - \phi(x,0)) \\ &= -\frac{2}{dy}(\phi(x,1) - \phi(x,0)) - \frac{dy^2}{6}(\partial_{yyy}\phi(x,\xi_1) + \mathcal{O}(\Delta_y^3) \end{aligned}$$

where $\xi_1 \in [y_0, y_1]$. Thus, we finally obtain

$$A + E(x,0) + E(x,1) = -\frac{2}{dy}(\phi(x,1) - \phi(x,0)) + \frac{dy^2}{6}\frac{\partial^2}{\partial y^2}E(x,\xi_1) + \mathcal{O}(\Delta_y^3)$$

Moreover, classical quadrature theory gives us the existence of $\xi_2 \in [y_0, y_1]$ such as

$$\int_{y_0}^{y_1} E(x,y)dy = \frac{dy}{2}(E(x,0) + E(x,1)) - \frac{dy^3}{12}\frac{\partial^2}{\partial y^2}E(x,\xi_2).$$

Replacing $E(x,\xi_1)$ by $E(x,\xi_2)$, which is of first order in our computation leads to

$$A + E(x,0) + E(x,1) = -\frac{2}{dy}(\phi(x,1) - \phi(x,0)) - \frac{2}{dy}\int_{y_0}^{y_1} E(x,y)dy + (E(x,0) + E(x,1)) + \mathcal{O}(\Delta_y^3)$$

so that $A = \mathcal{O}(\Delta_y^3)$ which is what was expected.

References

[1] R. Barthelmé, *Le problème de conservation de la charge dans le couplage des équations de Vlasov et de Maxwell*, Thèse de l'Université Louis Pasteur, 2005.

[2] N. Besse, M. Mehrenberger, *Convergence of classes of high order semi-Lagrangian schemes for the Vlasov-Poisson system*, Math. Comput., **77**, pp. 93-123, (2008).

[3] C.K. Birdsall, A.B. Langdon, *Plasma Physics via Computer Simulation*, Inst. of Phys. Publishing, Bristol/Philadelphia, 1991.

[4] J.-A. Carillo, F. Vecil, *Non oscillatory interpolation methods applied to Vlasov-based models*, SIAM Journal of Sc. Comput. **29**, pp. 1179-1206, (2007).

[5] C. Z. Cheng, G. Knorr, *The integration of the Vlasov equation in configuration space*, J. Comput. Phys, **22**, pp. 330-3351, (1976).

[6] C.J. Cotter, J. Frank, S. Reich *The remapped particle-mesh semi-Lagrangian advection scheme,* Q. J. Meteorol. Soc., **133**, pp. 251-260, (2007)

[7] J. Denavit, *Numerical simulation of plasmas with periodic smoothing in phase space*, J. Comput. Phys., **9**, pp. 75-98, 1972.

[8] F. Filbet, E. Sonnendrücker, P. Bertrand, *Conservative numerical schemes for the Vlasov equation*, J. Comput. Phys., **172**, pp. 166-187, (2001).

[9] F. Filbet, E. Sonnendrücker, *Comparison of Eulerian Vlasov solvers*, Comput. Phys. Comm., **151**, pp. 247-266, (2003).

[10] B. D. Fried, S. D. Comte, *The plasma dispersion function*, Academic Press, New York, 1961.

[11] A. Ghizzo, P. Bertrand, M.L. Begue, T.W. Johnston, M. Shoucri, *A Hilbert-Vlasov code for the study of high-frequency plasma beatwave accelerator*, IEEE Transaction on Plasma Science, **24**, p. 370, (1996).

[12] V. Grandgirard, M. Brunetti, P. Bertrand, N. Besse, X. Garbet, P. Ghendrih, G. Manfredi, Y. Sarrazin, O. Sauter, E. Sonnendrücker, J. Vaclavik, L. Villard, *A drift-kinetic semi-Lagrangian 4D code for ion turbulence simulation*, J. Comput. Phys., **217**, pp. 395-423, (2006).

[13] W. Magnus, S. Winkler, *Hill's equation*, John Wiley and sons, (1966).

[14] R.D. Nair, J.S. Scroggs, F. H.M. Semazzi, *A forward-trajectory global semi-Lagrangian transport scheme*, J. Comput. Phys., **190**, pp. 275-294, (2003).

[15] T. Nakamura, T. Yabe, *Cubic interpolated propagation scheme for solving the hyper-dimensional Vlasov-Poisson equation in phase space*, Comput. Phys. Comm., **120**, pp. 122-154, (1999).

[16] S. Reich, *An explicit and conservative remapping strategy for semi-Lagrangian advection*, Atmospheric Science Letters **8**, pp. 58-63, (2007).

[17] M. Shoucri, *A two-level implicit scheme for the numerical solution of the linearized vorticity equation*, Int. J. Numer. Meth. Eng. **17**, p. 1525 (1981).

[18] A. Staniforth, J. Cot, *Semi-Lagrangian integration schemes for atmospheric models - A review*, Mon. Weather Rev. **119**, pp. 2206-2223, (1991).

[19] E. Sonnendrücker, J. Roche, P. Bertrand, A. Ghizzo *The semi-Lagrangian method for the numerical resolution of the Vlasov equation,* J. Comput. Phys., **149**, pp. 201-220, (1999).

[20] S. Vadlamani, S. E. Parker, Y. Chen, C. Kim, *The particle-continuum method: an algorithmic unification particle in cell and continuum methods*, Comput. Phys. Comm. **164**, pp. 209-213, (2004).

[21] M. Zerroukat, N. Wood, A. Staniforth, *A monotonic and positive-definite filter for a Semi-Lagrangian Inherently Conserving and Efficient (SLICE) scheme*, Q.J.R. Meteorol. Soc., **131**, pp 2923-2936, (2005).

[22] M. Zerroukat, N. Wood, A. Staniforth, *The Parabolic Spline Method (PSM) for conservative transport problems*, Int. J. Numer. Meth. Fluids, **51**, pp. 1297-1318, (2006).

Centre de recherche INRIA Nancy – Grand Est
LORIA, Technopôle de Nancy-Brabois - Campus scientifique
615, rue du Jardin Botanique - BP 101 - 54602 Villers-lès-Nancy Cedex (France)

Centre de recherche INRIA Bordeaux – Sud Ouest : Domaine Universitaire - 351, cours de la Libération - 33405 Talence Cedex
Centre de recherche INRIA Grenoble – Rhône-Alpes : 655, avenue de l'Europe - 38334 Montbonnot Saint-Ismier
Centre de recherche INRIA Lille – Nord Europe : Parc Scientifique de la Haute Borne - 40, avenue Halley - 59650 Villeneuve d'Ascq
Centre de recherche INRIA Paris – Rocquencourt : Domaine de Voluceau - Rocquencourt - BP 105 - 78153 Le Chesnay Cedex
Centre de recherche INRIA Rennes – Bretagne Atlantique : IRISA, Campus universitaire de Beaulieu - 35042 Rennes Cedex
Centre de recherche INRIA Saclay – Île-de-France : Parc Orsay Université - ZAC des Vignes : 4, rue Jacques Monod - 91893 Orsay Cedex
Centre de recherche INRIA Sophia Antipolis – Méditerranée : 2004, route des Lucioles - BP 93 - 06902 Sophia Antipolis Cedex

Éditeur
INRIA - Domaine de Voluceau - Rocquencourt, BP 105 - 78153 Le Chesnay Cedex (France)
http://www.inria.fr
ISSN 0249-6399